Acta Materialia 203 (2021) 116483

Contents lists available at ScienceDirect

Acta Materialia

journal homepage: www.elsevier.com/locate/actamat

Carbon nanotube (CNT) metal composites exhibit greatly reduced radiation damage

Penghui Cao[b,1], Kang Pyo So[a,1], Yang Yang[a,f], Jong Gil Park[c], Mingda Li[a], Long Yan[d], Jing Hu[e], Mark Kirk[e], Meimei Li[e], Young Hee Lee[c], Michael P. Short[a,*], Ju Li[a,g,*]

[a] Department of Nuclear Science and Engineering, Massachusetts Institute of Technology, 77 Massachusetts Ave., Cambridge, MA 02139, USA
[b] Department of Mechanical and Aerospace Engineering, University of California, Irvine, Irvine, CA 92697, USA
[c] IBS Center for Integrated Nanostructure Physics, Institute for Basic Science, Sungkyunkwan University 440-746, Republic of Korea
[d] Shanghai Institute of Applied Physics, Chinese Academy of Sciences, Shanghai 201800, China
[e] Nuclear Science and Engineering Division, Argonne National Laboratory, Lemont, IL, 60439, USA
[f] National Center for Electron Microscopy, Molecular Foundry, Lawrence Berkeley National Laboratory, 67 Cyclotron Rd, Berkeley, CA 94720, USA
[g] Department of Materials Science and Engineering, Massachusetts Institute of Technology, 77 Massachusetts Ave., Cambridge, MA 02139, USA

ARTICLE INFO

Article history:
Received 22 July 2020
Revised 18 October 2020
Accepted 9 November 2020
Available online 14 November 2020

Keywords:
ion irradiation
IVEM
carbon nanotubes
nuclear materials
in situ
defects

ABSTRACT

Radiation damage of structural materials leads to mechanical property degradation, eventually inducing failure. Secondary-phase dispersoids or other defect sinks are often added to materials to boost their radiation resistance. We demonstrate that a metal composite made by adding 1D carbon nanotubes (CNTs) to aluminum (Al) exhibits superior radiation resistance. *In situ* ion irradiation with transmission electron microscopy (TEM) and atomistic simulations together reveal the mechanisms of rapid defect migration to CNTs, facilitating defect recombination and enhancing radiation tolerance. The origin of this effect is an evolving stress gradient in the Al matrix resulting from CNT transformation under irradiation, and the stability of resulting carbides. Extreme value statistics of large defect behavior in our simulations highlight the role of CNTs in reducing accumulated damage. This approach to controlling defect migration represents a promising opportunity to enhance the radiation resistance of nuclear materials without detrimental effects.

1. Introduction

A common tactic when designing radiation-resistant nanomaterials [1] is to engineer stable defect sinks to absorb radiation-induced microstructural defects. Oxide-dispersion strengthened steels (ODS) [2] and Cu-Nb multilayers [3] are well-known examples of radiation-tolerant nano-structured materials. The former is strengthened by "0D" microstructural features (oxide nanoparticles with near-unity aspect ratio), while the latter is strengthened by "2D" ones. In both cases phase boundaries are the main venues for radiation defect recombination and annihilation, but the topological characteristics of these sinks are different. In "0D" features, phase boundaries are isolated and do not percolate, while in "2D" features, the boundaries are extensive in two directions and percolate in space. Such a classification is important to consider, as many forms of damage are highly sensitive to flaw size and topology. For example, a 2D crack (oblate ellipsoid with aspect ratio $\rightarrow \infty$) is the ultimate form of damage, because of the high stress concentration allowing its propagation at low bulk stresses. A single void or even a long, needle-shaped void (prolate ellipsoid with aspect ratio $\rightarrow \infty$) by contrast would be less dangerous from this linear elastic fracture mechanics viewpoint, because no divergence in stress amplification factor would develop [4]. When helium accumulates on 2D sinks, such as a percolating grain boundary (GB) network or a crack face, it generally compromises the mechanical integrity significantly when subjected to tensile stress (Fig. 1A). If such damaging evolution could be confined to even a percolating network of 1D sinks (Fig. 1B), it would be far less detrimental to material properties.

The classic example of 1D percolating sinks would be the dislocation tangle, since we know dislocation cores absorb vacancies and interstitials by climb. However, it is well known that dislocations, despite being 1D defects common to all crystalline materials, are in effect "erased" by even low levels of irradiation [5]. It is nonetheless interesting to observe that 1D features generally

* Corresponding authors.
E-mail addresses: caoph@uci.edu (P. Cao), hereiam@mit.edu (M.P. Short), liju@mit.edu (J. Li).
[1] Authors contributed equally to this work.

https://doi.org/10.1016/j.actamat.2020.116483
1359-6454/

percolate in space if dense enough, because a dislocation cannot freely terminate inside a crystal (Frank's rule) and must connect to other dislocations. In this aspect it is the same for GB networks, which provide percolating paths for (n, α)-produced helium gas to escape. Compared with 2D/3D defects (the latter of which have 2D interfaces), 1D features do not generally induce huge stress amplifications. Herein lies the inherent advantage of 1D microstructural sinks - they can remove damage without inducing excessive stress concentrations themselves. It is noted that 1D carbon nanotubes (CNTs) and ceramic nanowires (NWs) have been successfully dispersed in metallic alloys [6]. They can be well-dispersed in metal grain interiors and can be considered, in the ideal limit, as uniform tangles. Such 1D metal nanocomposites have been economically mass-produced at the commercial scale [7], and they have unique mechanical properties at both room- and high-temperatures [8]. At room-temperature, the dispersed CNTs can enhance the metal's tensile strength by as much as 50% with just 1 vol. % addition, without sacrificing tensile ductility due to Taylor dispersion hardening. High-temperature creep strength is also accordingly enhanced, because mobile dislocations cannot react to remove 1D dispersions, whereas they can react with and remove 1D forest dislocations in a process known as dislocation recovery. At both room- and high-temperatures, the 1D dispersion network does not pose an immediate risk for fracture, as long as their diameter stays below about 10 nm [9].

A host of new, potential issues arise when considering the effects of radiation damage on 1D dispersions in metal nanocomposites. First, multi-walled CNTs can ballistically mix and then react with the host metal atoms, forming metal carbide (M_xC) dispersions in place of CNTs. Fortunately these M_xC dispersions can maintain the 1D morphology of the original nanotube, like a fossil, and the M_xC/Metal interfaces can still maintain robust sinking capability like the previous CNT/metal interfaces [10]. An interesting issue is the transformation strain of such radiation-enhanced phase change. We will show that a contractile transformation strain is generated as CNTs form M_xC carbides with an Al matrix, which in turn induces tensile stress in the metal around the precipitate. This $1/r^2$ tensile stress, where r is distance from the interface, will cause radiation-induced point defects, specifically self-interstitials, vacancies, and helium, to quickly diffuse to this percolating network of self-generated M_xC nanowires.

We present *in situ* TEM ion radiation and atomistic simulation studies of a 1D dispersion strengthened Al-CNT composite alloy to elucidate the role of CNTs at ameliorating radiation damage. We found that 1D CNTs lower the radiation defect volume fraction in Al-CNT by nearly one order of magnitude compared with pure Al, and extreme value (EV) statistical analysis of the largest defects shows far smaller defect clusters even after heavy irradiation. Importantly, defect migration displays a clearly directional path towards CNTs, where they react to facilitate recombination, alleviating radiation-induced damage. The biased defect diffusional behavior is related to the tensile stress gradient field produced by chemical transformation of carbon-metal system under radiation.

2. Methods

2.1. Al-CNT composite fabrication

A uniform, intragranular dispersion of CNTs into an Al matrix was obtained by using powder metallurgy under non-oxidizing conditions, including (step 1) CNT declustering on the surface of Al particles, (step 2) cold welding and encapsulation of dispersed CNTs and further consolidation into Al particles to form Al–C covalent bonds by spark plasma sintering (SPS), and (step 3) extrusion. A good intragranular dispersion of 1D strengtheners is critical for the enhancement of composite properties. This involves encapsulation of CNTs inside Al grains via surface diffusion-driven cold welding, enabling close interaction between CNTs and radiation defects in metals. *In situ* transmission electron microscopy (TEM) demonstrates liquid-like envelopment of CNTs into Al nanoparticles by cold-welding [10]. Experimental parameters used in this study are described in the Supplementary Information. Al-CNT samples with thicknesses of ~100 nm were prepared using a focused ion beam (FIB, Helios Nanolab 600 Dual Beam), transferred onto Cu half-grids using an Omniprobe, and welded by electron beam deposition of platinum via a Pt-bearing precursor gas inside a scanning electron microscope.

2.2. In situ *irradiation experiments*

In situ Kr^{2+} ion irradiation at 100 keV and 1 MeV was performed on pure Al and Al-CNT composites at room temperature in the Intermediate Voltage Electron Microscope (IVEM) at the Argonne National Laboratory, where an ion accelerator is attached to a Hitachi H-9000NAR microscope. Kr^{2+} ion irradiation was performed on FIB-extracted TEM lamellae (irradiation conditions are listed in table S1). The microscope was operated at 150 kV, and kept on during irradiation. The dose rate was 0.9 to 2.7×10^{-3} DPA/s. A CCD camera was used to capture microstructural evolution during irradiation at fifteen frames per second. The Stopping power and Range of Ions in Matter (SRIM) [11] simulation package was used to estimate the damage displacement profile and the Kr^{2+} injected ion distribution.

2.3. Molecular dynamics simulations of radiation damage

A simulation cell size of $12.2 \times 12.2 \times 12.2$ nm^3 containing 108,000 Al atoms was used. For the Al-CNT system, we first created a CNT with a diameter of 1.35 nm, a length of 12.2 nm, and 2,000 C atoms. A cylindrical hole with a diameter of 1.64 nm parallel to the z-axis was created in the Al to embed the CNT. The interaction between Al-Al atoms was described by an EAM (Embedded-Atom Method) potential [12], while the second-generation REBO potential [13] was used to model C-C interaction, and a typical 12-6 Lennard-Jones potential was adopted to describe the interaction between Al and C [7]. Before each radiation damage simulation, we first relaxed the system to zero pressure employing a Nosé-Hoover isothermal-isobaric ensemble [14] at 300K for 50 ps, with periodic boundary conditions applied in all three directions. We simulated multiple, consecutive, self-ion radiation damage cascades and tracked defect nucleation, migration, and annihilation arising from them [15]. To properly represent high-energy ion collisions, a Ziegler-Biersack-Littmark (ZBL) repulsive potential [16] was smoothly joined to the aforementioned potentials [17], and an adaptive timestepping algorithm was used to limit atomic movement to 0.005 nm per timestep. For each displacement cascade, an Al atom was randomly chosen as the primary knock-on atom (PKA), and the entire system was shifted to position of the PKA as the center of the system. This prevents damage cascades from reaching the simulation boundaries in all cases. A kinetic energy of 5 keV was assigned to the PKA with a random incident direction, and 50,000 adaptive timesteps were performed. The Nosé-Hoover temperature-rescaling thermostat [18,19] was applied to the atoms at the sides of the simulation cell with a width of half a lattice constant, mimicking a thermal sink to absorb excess collision energy and cool the system to 300K between cascades. The cascade simulation procedure was repeated with randomly chosen PKAs to simulate spatially random damage cascades. A damage level of ~0.94 DPA was achieved according to the NRT formula [20]. To illustrate defect evolution during collision cascades, we used adaptive common neighbor analysis [16] and the Wigner-Seitz cell

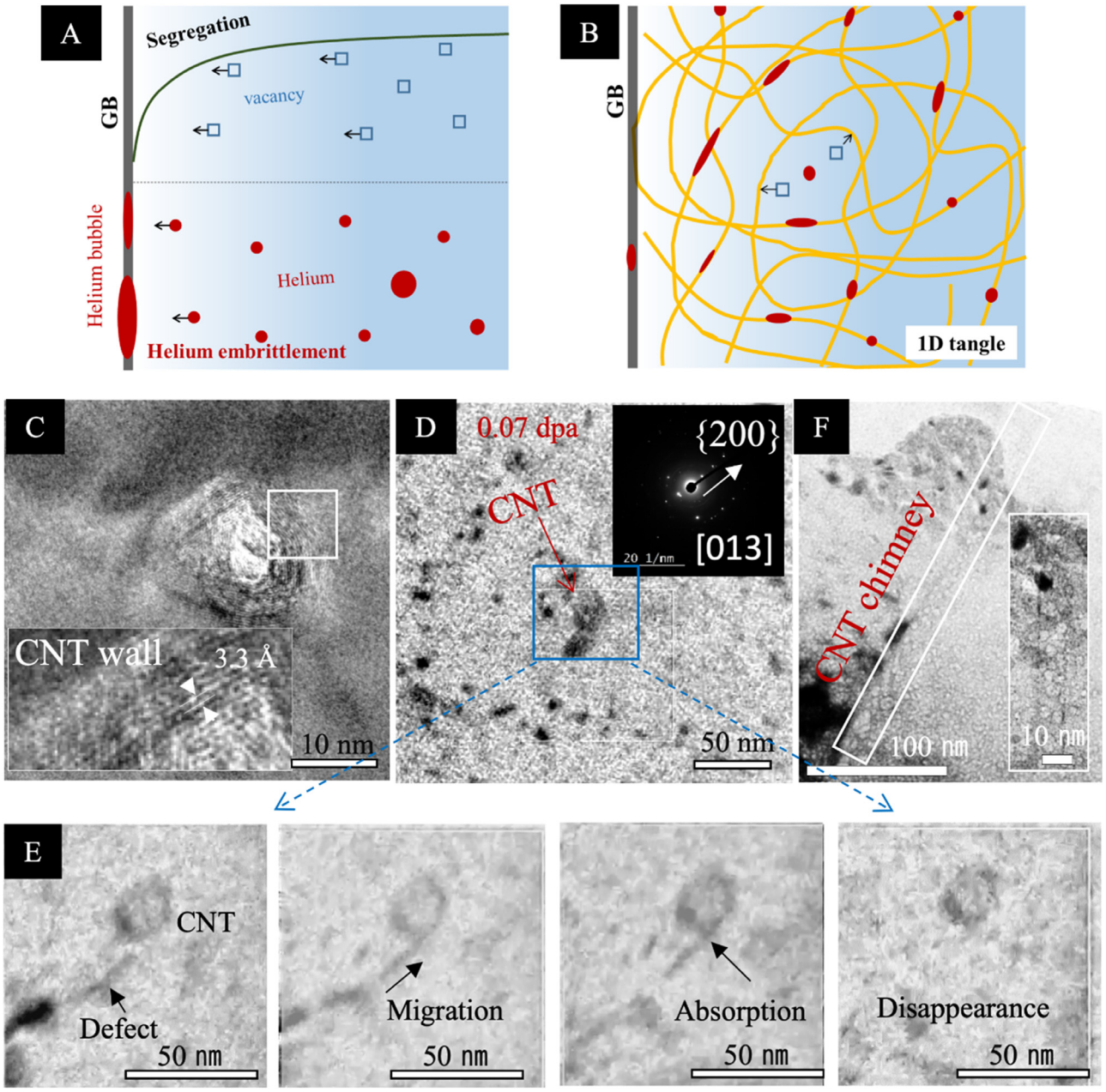

Fig. 1. (A) Schematic illustration of GB-related radiation degradation such as radiation-induced segregation and helium gas embrittlement. The green line indicates the concentration of vacancies away from the GB. (B) 1D tangles of CNTs or NWs accommodate radiation defects and protect GB integrity. In (C-D), we demonstrate the role of CNTs in attracting radiation defects. (C) Intact wall structure of a CNT in an Al grain before irradiation, and (D) defect distribution near a CNT at 0.07 DPA. (E) TEM image sequence showing the migration, evolution, and annihilation of defects during irradiation (blue box in (B)). (F) Large helium bubbles accumulated alongside a CNT channel (the inset shows an enlarged view of the CNT region).

method to identify defective (non-FCC) structures and Frenkel pairs (interstitial and vacancy), respectively.

3. Results

3.1. Radiation defect migration and annihilation near 1D-CNTs

The dispersion of CNTs within Al grains was prepared using surface diffusion-driven cold-welding [8]. The intact wall structure of CNTs with a 3.3 Å interlayer carbon spacing is shown in Fig. 1C, indicating its solid structural integrity with the surrounding Al matrix. Prior to ion irradiation, we observed a moderate density of intrinsic defect loops in TEM (3.6×10^{21} m^3 in pure Al and 7.0×10^{21} m^3 in Al-CNT) generated during sample preparation. The range of defect densities is comparable to that in coarse grained Ag ($\sim 10^{21}$ m^3) [8,21]. The excess defects in Al-CNT are believed to result from the generation of micro-strain near CNTs, due to lattice mismatch, differing thermal expansion coefficients [6] between Al and carbon, and the FIB specimen removal process. During *in situ* ion radiation defects and small clusters appear, migrate, react with each other, and eventually annihilate near the CNT. An example of dynamic defect nucleation and evolution is shown in Movies 1-2, as well as in Fig. 1. In Fig. 1D, we show the defect distribution near a CNT at a low irradiation dose of 0.07 DPA (displacements per atom). With increasing irradiation dose, we readily observe the migration of defects towards the CNT, where they further interact

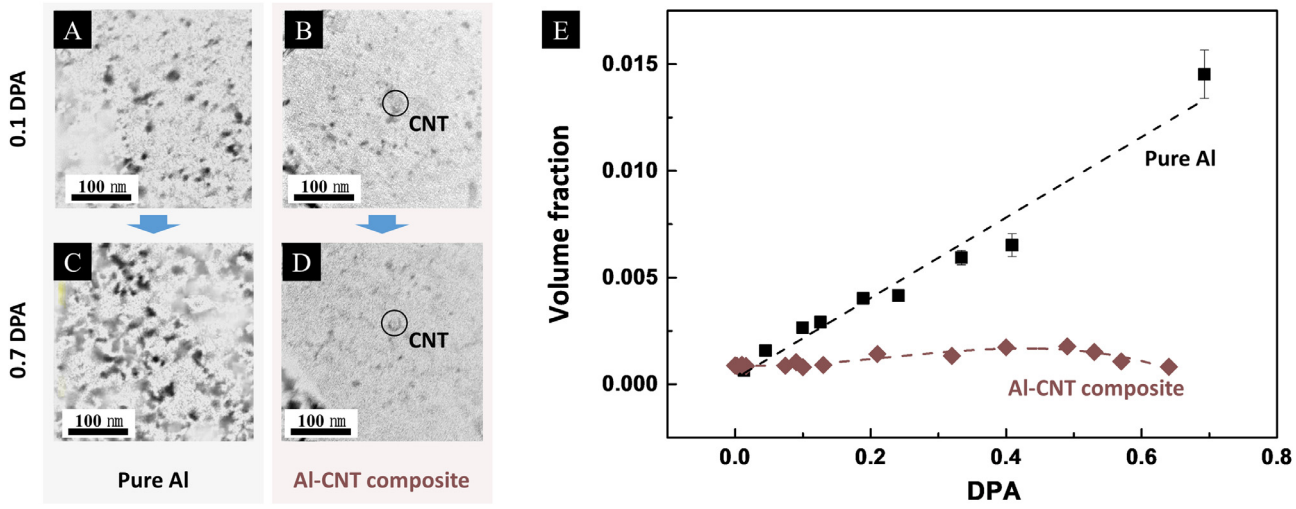

Fig. 2. Microstructural evolution after 0.10 DPA irradiation of (A) pure Al and (B) Al-CNT composite, and 0.69 DPA irradiation of (C) pure Al and (D) Al-CNT. The black dots represent the defects and the black circles highlight the location of the CNT. (E) Volume fraction of radiation defect clusters as a function of radiation dose.

with it, and are finally absorbed and disappear (Fig. 1E). The motion of defects exhibits non-random walk migration characteristics [22], showing a drift towards the CNT. This biased transport behavior shows how the CNT alters bulk defect migration pathways, as would be expected from any strong microstructural damage sink. In addition to self-defects, we found that the CNTs alter helium bubble nucleation and growth as shown in Fig. 1F, where large helium bubbles concentrate and align along the 1D CNT channel.

3.2. Spatio-temporal evolution of defects in Al and Al-CNT under irradiation

Microstructural evolution of pure Al and Al-CNT as a function of irradiation dose up to 0.7 DPA are analyzed and compared next. The radiation response of Al-CNT differs markedly from that of pure Al in terms of defect size and density. In Al, the number and size of defects drastically increases from 0.1 DPA (Fig. 2A) to 0.7 DPA (Fig. 2C), whereas the Al-CNT composite exhibits much fewer and smaller defects (Fig. 2B & D). The effect of CNTs on radiation damage reduction can also be seen in Fig. 2E, where we present the defect volume fraction as a function of radiation dose. The volume fraction in Al shows a steady increase with dose, reaching 0.015 at 0.69 DPA, while in our Al-CNT composite it is lowered by nearly one order of magnitude at 0.64 DPA. Defect sizes and quantities are quantified by statistics over many frames to different DPA, which exhibit less deviation with the type and energy of ion/neutron irradiation [23]. Defect clusters as small as 5 nm were identified, while defects smaller than 3 nm were difficult to identify in the TEM.

In Fig. 3A, we show the evolution of defect size distributions with radiation dose. The trend of increased defect sizes in pure Al is clearly visible with increasing irradiation dose (Fig. 3A), with a maximum defect cluster size of 35 nm at 0.69 DPA. In contrast, the Al-CNT shows a nearly constant defect size of around 5 nm, with some of the defects growing after 0.21 DPA then shrinking in size (right panel of Fig. 3A). From a fracture mechanics perspective, the large defects should be more detrimental to mechanical integrity than small ones, and crucial in defining radiation-induced material degradation and failure. We apply extreme value theory [24] to analyze defect size data and deduce the tail of the distribution of the underlying, unknown defect distributions in pure Al and the Al-CNT composite. The extreme defect distributions, which are of central interest, are calculated by generalized extreme value (GEV) functions, giving rise to different behaviors in Al and Al-CNT (see Supplementary materials). The GEV distribution of Al with its large shape parameter ξ implies that the underlying defect distribution has a heavy tail such as that seen in a power-law decay, which is inconsistent with radiation experiments [25]. In Al-CNT, the tail feature shows a clear tendency from slow power-law to fast Gaussian-like decay, suggesting high radiation-resistance to large defects. In Fig. 3B, we show cumulative density distributions of extreme defects with the calculated GEV functions. In addition, one can see that large defects are more frequent and decay more slowly in Al than that in Al-CNT.

To uncover the effects of CNTs on radiation defect evolution, we show the average defect contrast as a function of distance away from a CNT in Fig. 3C. When increasing the dose from 0.40 to 0.64 DPA, the peak defect region shifts closer to the CNT, indicating the preferential drift of defects towards it. Defects with biased migration likely gather near the CNT, which promotes recombination within the realm of its stress field, giving rise to a lower defect density and higher damage tolerance. Owing to CNT-assisted defect recombination, the defect density near a CNT (within 50 nm), which is measured in the same grain, is one third of that far from a CNT (>50 nm). The lower defect density close to the CNT can be correlated to defect migration towards the CNT and its eventual disappearance, previously shown in Fig. 1C-F.

3.3. Molecular dynamics simulations of radiation damage evolution and annihilation in Al-CNT

MD simulations of consecutive radiation damage cascades reveal the mechanisms behind damage reduction in Al-CNT composites. A high dose of ~1 DPA can be directly simulated to compare with the aforementioned irradiation experiments. In Fig. 4A, we present the number of radiation defects (Frenkel pairs) as a function of DPA in Al and Al-CNT. It can be seen that the Al-CNT exhibits an initial rise in defect populations up to ~0.1 DPA. After that, the number of defects essentially saturates with a total of ~400 defects per 108,530 atoms in the simulation cell. In contrast, the defects produced in pure Al continue to build up through the simulated damage level of 1 DPA, showing no sign of abating even though the defect accumulation rate is smaller after ~0.2 DPA. Our simulation results of damage in Al and Al-CNT demonstrate good

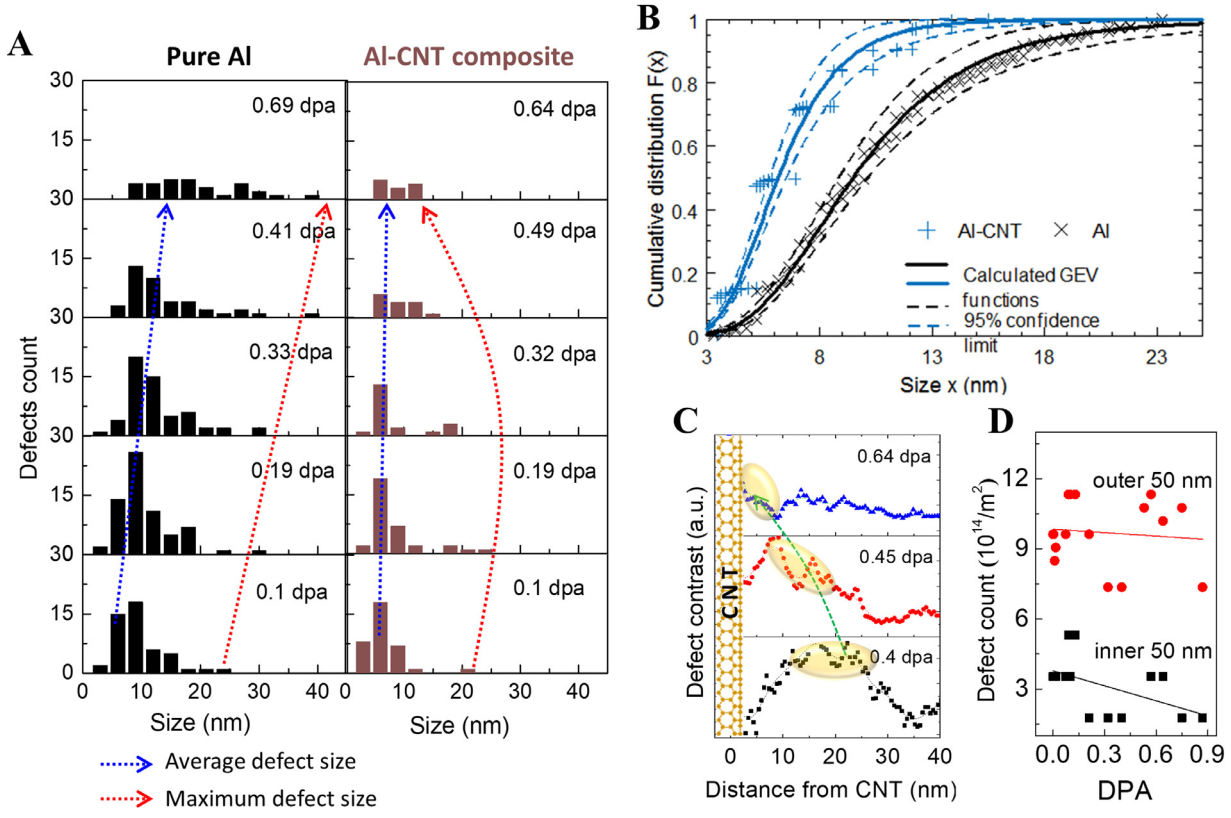

Fig. 3. (A) Size distribution of defects in pure Al and Al-CNT composite following irradiation, showing that the Al exhibits larger defects with continued irradiation, while defect sizes remain small in Al-CNT. The defects were counted over an area of $14.5 \times 10^4\ nm^2$ in Al and $4.6 \times 10^4\ nm^2$ in Al-CNT. (B) Extreme value statistics of defect size in Al and Al-CNT. The solid lines are calculated GEV functions with 95% confidence intervals outlined by the dashed lines. (C) Defect contrast near CNTs at radiation doses of 0.40, 0.45, and 0.64 DPA. The peak shift with increasing DPA shows the migration of defects toward the CNT. (D) Defect cluster density evolution in the Al-CNT composite in two regions, within 50 nm from the CNT (inner 50 nm) and away from this region (outer 50 nm). Defect densities are significantly lower in the inner 50 nm than in the outer region.

agreement with the *in situ* irradiation experiments in Fig. 2E. More importantly, defect migration shows a preferential drift towards CNTs, agreeing with the earlier assertion that 1D CNTs alter the migration energy landscape to cause defects to converge towards the CNTs (see Movie 3).

The details of defect evolution during radiation damage are presented in Fig. 4B, where the defect size distributions and their statistics are shown at various doses. At a low dose of 0.07 DPA, both pure Al and the Al-CNT composite show very similar distributions, and only small defects (less than 300 atoms) appear. As the DPA increases, the large defective structures in pure Al grow significantly in size, while those in the Al-CNT composite do not appear to do so. Specifically, clusters containing more than 500 defects appear in pure Al at 0.29 DPA, continuing to grow at doses from 0.58 to 0.94 DPA. Compared with pure Al at 0.94 DPA, the Al-CNT composite clearly exhibits much smaller defect clusters. This observation further supports what was observed and asserted in our experiments.

Figs. 4D-E show the spatial distributions of defect clusters in the two materials, and their evolution with increasing DPA. At a dose of 0.015 DPA, the two materials show no visible difference in defect sizes with only small defects appearing randomly in the system. At 0.43 DPA, a planar interstitial cluster has nucleated in Al, and its size continues to grow even at 0.94 DPA (Fig. 4D). Such a large defect is unfavorable in the presence of a CNT as shown in Fig. 4E, where the distribution of defect clusters undergoes no changes from 0.43 to 0.94 DPA. The comparison between pure Al and Al-CNT indicates that the presence of a CNT in Al reduces both the number and sizes of radiation defects, implying higher radiation-induced damage resistance.

4. Discussion

4.1. Thermodynamic bias to remove radiation damage

The relatively long-range migration of defects towards CNT interfaces suggests possible thermodynamic driving forces. A non-uniform field can support such a driving force, such as a gradient in mechanical stress or defect density. During irradiation, the Al atoms collide with nearby CNTs due to displacement cascades, which result in the formation of Al-C atomic bonds (Fig. 5A). This continuous buildup of chemical bonds leads to a high density of aluminum carbides, causing volumetric contraction and tensile strain focused on each former CNT site (Fig. 5B). For instance, a 12.56% volume contraction would arise by forming Al_4C_3.

A long-range tensile stress field is produced and maintained by the Elshelby inclusion-like transformation [26], with an analytical solution of $\sigma_{rr} \propto a^2/r^2$, where σ_{rr} is the stress along the radial direction, a represents the aluminum carbide inclusion diameter, and r is the distance from the inclusion center (see Supplementary materials). It is interesting to note that both interstitial and vacancy defects in Al have positive relaxation volumes $\Omega^{\text{relax}}_{\text{defect}}$ [27], which cause local compressive stress fields. If this negative strain-volume of defects is anisotropic, which is the case for interstitial-type defects and vacancy clusters, such defects will align with the stress gradient, driving them toward the positively stressed region described by

$$\mathbf{J}_{\text{defect}} = -c_{\text{defect}} M_{\text{defect}} [(\nabla P)\Omega^{\text{relax}}_{\text{defect}} + k_B T \ln c_{\text{defect}}], \quad (1)$$

where $c_{\text{defect}}(\mathbf{x})$ is the concentration of the defect, M_{defect} is the mobility of the defect, and $P(\mathbf{x})$ is the spatially dependent pres-

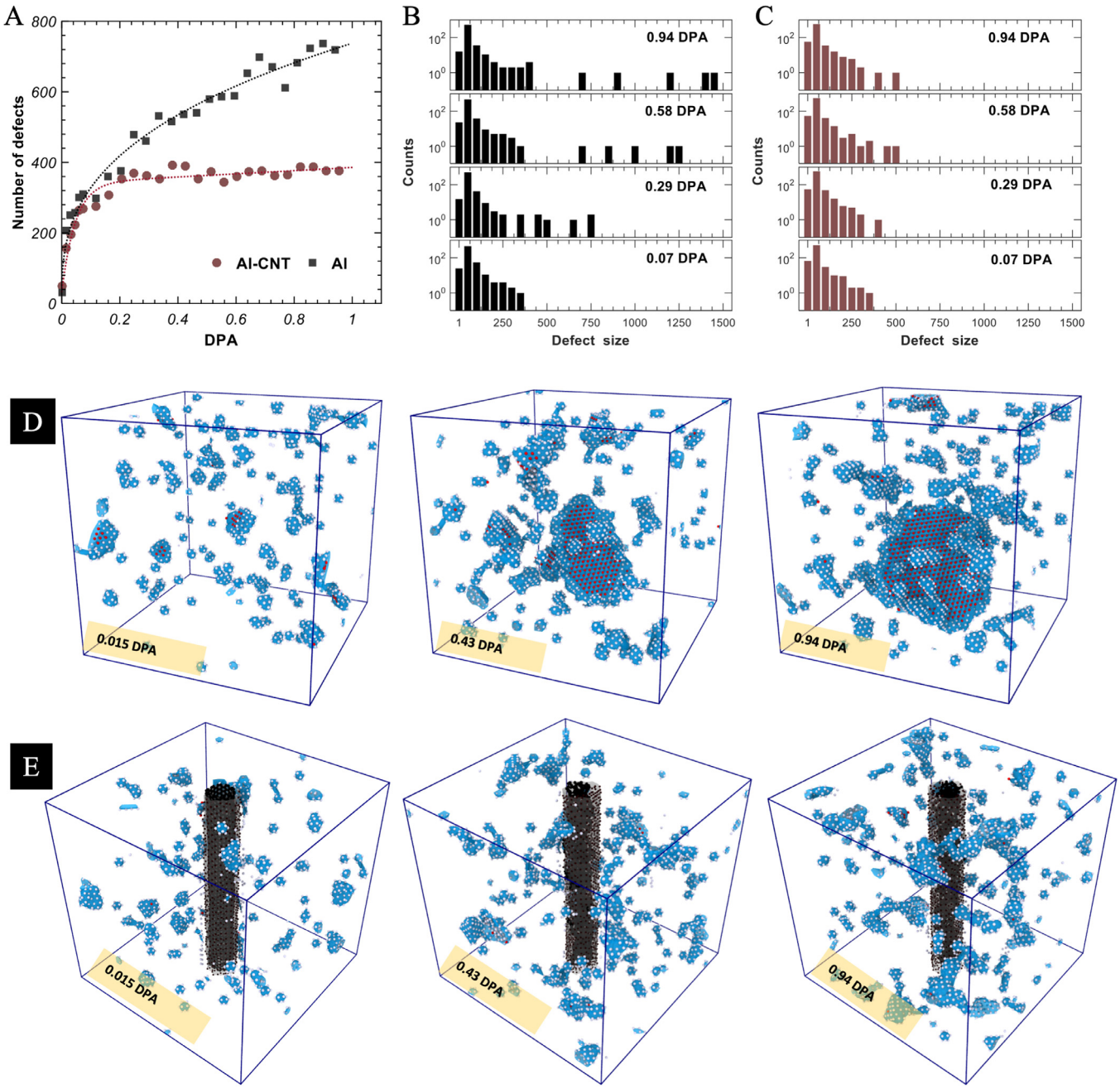

Fig. 4. (A) Total number of irradiation-induced vacancy and interstitial defects as a function of DPA for pure Al and Al-CNT. Defect size distributions at various radiation doses are shown in (B) for Al and (C) for Al-CNT. The defect size is measured by the number of atoms with a different number of bonds than the surrounding crystal structure. The data are collected from five independent simulations. (D, E) Evolution of defect structures in pure Al and Al-CNT, respectively. Only non-FCC atoms are shown, selected by coordination number analysis.

sure. The effect of ∇P applies an attractive force on both radiation-induced vacancies and interstitials, driving them to migrate towards each Al-carbide as shown in Fig. 5C. In addition to the stress gradient, there is another driving force provided by defect density heterogeneity. As shown in Fig. 3D, the outer region (>50 nm) has a defect density almost three times higher than that found in the inner 50 nm. The density gradient of defects drives them from the high density outer region to the low density inner region, promoting defect-biased migration as seen in both our simulations and our experiments. When defects move closer to a CNT, interstitial- and vacancy-type defects recombine, reducing the free energy of the system.

4.2. Similarities and differences between 1D CNTs and other dispersoids

The experiments and simulations show that CNTs play a key role in annihilating radiation damage in the grain interior, by facilitating defect recombination at or near the heterogeneous interface of the Al-CNT or the subsequent Al-carbide. The diffusive behavior of defects near CNTs exhibits biased migration, converging to the CNT (Fig. 5C) much like other strong radiation defect sinks, such as GBs in nanocrystalline materials [22,28,29]. However, unlike the random walk-like diffusion mode in bulk metals [30], the long-range stress field induced by CNTs attracts both vacancies and in-

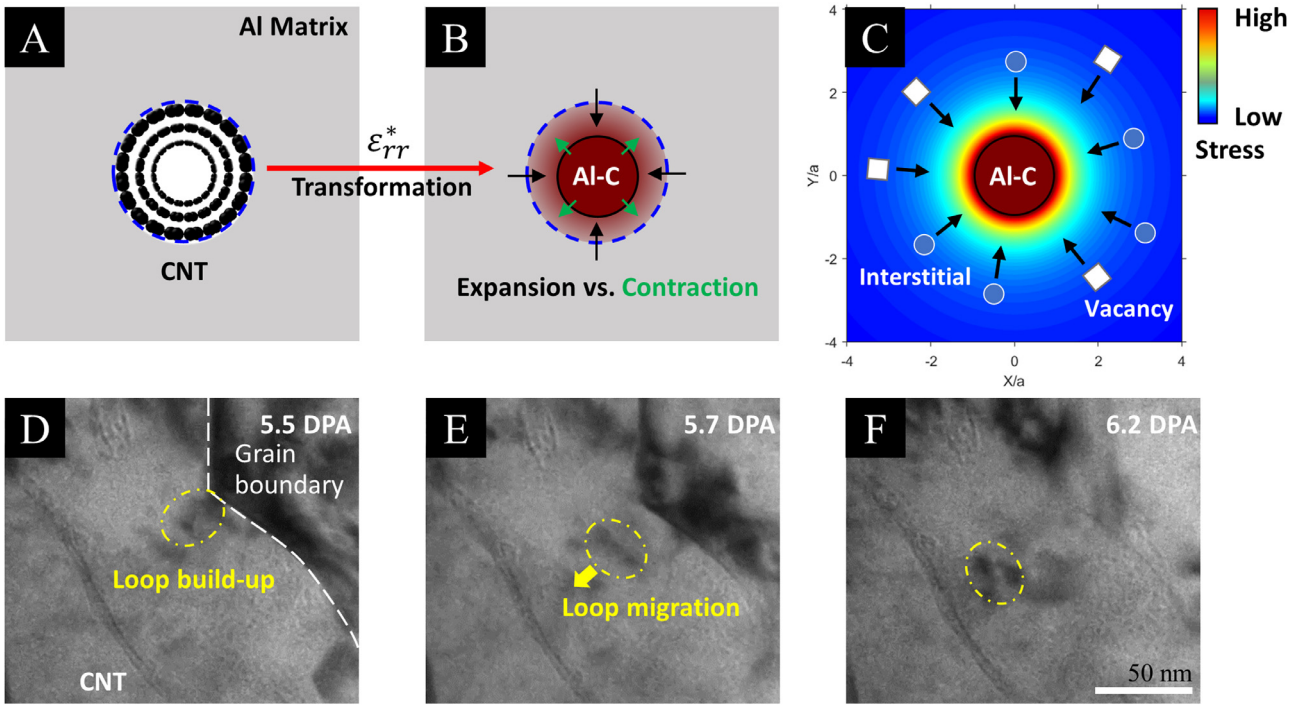

Fig. 5. (A-C) Tensile stress field induced by formation of Al_4C_3 and the resulting convergent defect migration mode. (A) Al and carbon atoms undergo a chemical reaction, forming high-density Al_4C_3. The eigenstrain ϵ^*_{rr} represents the volume shrinkage of the Al_4C_3 inclusion. (B) Both the Al matrix and Al_4C_3 inclusions experience tensile stress. (C) Convergent defect migration caused by the stress field gradient. The background is color-coded by the magnitude of radial stress, which decays with distance from the inclusion (diameter a) center proportional to $1/r^2$. (D-E) Experimental observation of defect migration between a CNT and a GB (Movie 4). (D) TEM of a CNT and a GB after saturation of vacancies and interstitials at 5.5 DPA, where defect loops build-up near the GB, and (E) and (F) show preferential defect loop migration to CNT.

terstitials. In this way CNTs behave as any other effective radiation damage sink should, continuously removing and inducing recombination of defects without being consumed or weakened themselves.

Unlike coherent or incoherent phase boundaries or even GBs [28], the mechanically and chemically robust CNT and subsequent Al-carbide generates a significant tensile stress gradient surrounding the interface produced by the radiation-induced phase transformation as discussed above. Due to the high diffusivity of interstitial-type defects, they accumulate near CNTs and serve as a local interstitial source to annihilate nearby and incoming vacancies, explaining the lower void density immediately near CNTs or Al-carbides. When radiation dose increases, interstitial aggregation and annihilation by recombining with incoming vacancies reaches a balanced state while maintaining a low degree of defect saturation, evidenced by the nearly constant defect density and size as shown in Fig. 2E. The effects of CNTs and GBs on defect reduction are directly compared in our *in situ* experiments shown in Fig. 5D-E and Movie~4 . At a high dose of ~5 DPA, the defect size and density near the CNT remains low with a cleaner microstructure, whereas many defect reactions can be seen occurring near the GB, including a number of defect clustering events followed by annihilation. At 5.5 DPA, a defect loop grown near the GB (Fig. 5D) can be seen slowly moving toward the CNT, demonstrating the strain-field biased preferential defect migration (Fig. 5E-F).

In addition to radiation-induced intrinsic defects, precipitation of helium bubbles is another major concern in nuclear energy systems, particularly in fusion reactors. The stress gradient in Al-CNT would guide the migration of helium atoms, accumulating them towards and along the lengths of CNTs (Fig. 1G). Furthermore, we observed the accumulation of heavy Kr^{2+} atoms at the interface in our *in situ* experiments, with a portion of them entering CNTs and finally disappearing (Movie~5). This observation shows that 1D nanotubes/nanowires can act as “nano-chimneys” (channels) to outgas helium and other gases while keeping their integrity.

The main purpose of this paper is demonstrating the concept of improving irradiation damage resistance through 1D interfaces. We introduce CNTs as a proven concept embodied in a 1D nanodispersion composite. As long as 1D nanodispersoids are stable at operating/processing temperatures and in their respective base materials (FCC, BCC, and HCP), this idea can and should be expanded to more nuclear-practical materials such as Zr, Ni, and Fe-based alloys. This could directly impact the cost and environmental footprint of nuclear energy, by making more dose-tolerant and robust nuclear structural materials. The difficulty which lies ahead is in the facile and repeatable dispersion of CNTs or similar dispersoids in these higher temperature base metals.

5. Conclusion

We present an Al-CNT composite which reduces radiation damage by one order of magnitude compared to pure, irradiated Al. *In situ* ion irradiation experiments and atomistic simulations together reveal the dynamic evolution and biased diffusion of radiation-induced defects to CNTs or subsequently formed Al-carbides, enhancing the recombination of defects and leading to high radiation tolerance. The preferential migration of defects towards CNTs is driven by the gradient of defect density and by the gradient of the long-range tensile stress field, caused by the formation of aluminum carbide at former CNT sites. The general design principle of using 1D nanodispersions in metallic matrix to avoid extreme stress concentration and damage accumulation represents a promising avenue new, enabling new nanocomposite materials with improved radiation tolerance.

Declaration of Competing Interest

The authors declare that they have no known competing financial interests or personal relationships that could have appeared to influence the work reported in this paper.

Acknowledgement

We acknowledge support from the US DOE Office of Nuclear Energy's NEUP Program under Grant No. DE-NE0008827, and from the US DOE Nuclear Science User Facilities (NSUF) for facility access via RPA-18-14783. The computational simulations made use of the resources of the High Performance Computing Center at Idaho National Laboratory, which is supported by the Office of Nuclear Energy of the U.S. DOE and the Nuclear Science User Facilities under Contract No. DE-AC07-05ID14517.

Supplementary material

Supplementary material associated with this article can be found, in the online version, at 10.1016/j.actamat.2020.116483

References

[1] I. Beyerlein, A. Caro, M. Demkowicz, N. Mara, A. Misra, B. Uberuaga, Radiation damage tolerant nanomaterials, Mater. Today 16 (11) (2013) 443–449.
[2] G. Odette, M. Alinger, B. Wirth, Recent developments in irradiation-resistant steels, Annu. Rev. Mater. Res. 38 (1) (2008) 471–503.
[3] M.J. Demkowicz, R.G. Hoagland, J.P. Hirth, Interface structure and radiation damage resistance in Cu-Nb multilayer nanocomposites, Phys. Rev. Lett. 100 (2008) 136102, doi:10.1103/PhysRevLett.100.136102.
[4] F. Nabarro, The strains produced by precipitation in alloys, Proc. R. Soc. Lond. A-Math. Phys. Sci. 175 (1940) 0519–0538.
[5] M. Makin, S. Manthorpe, The annealing of dislocation loops in neutron irradiated copper, Phil. Mag. 8 (94) (1963) 1725–1738.
[6] R. George, K. Kashyap, R. Rahul, S. Yamdagni, Strengthening in carbon nanotube/aluminium (CNT/Al) composites, Scr. Mater. 53 (10) (2005) 1159–1163.
[7] K.P. So, X.H. Liu, H. Mori, A. Kushima, J.G. Park, H.S. Kim, S. Ogata, Y.H. Lee, J. Li, Ton-scale metal-carbon nanotube composite: The mechanism of strengthening while retaining tensile ductility, Extreme Mech. Lett. 8 (2016) 245–250.
[8] K.P. So, A. Kushima, J.G. Park, X.H. Liu, D.H. Keum, H.Y. Jeong, F. Yao, S.H. Joo, H.S. Kim, H.N. Kim, J. Li, Y.H. Lee, Intragranular dispersion of carbon nanotubes comprehensively improves aluminum alloys, Adv. Sci. 5 (7) (2018) 1800115, doi:10.1002/advs.201800115.
[9] H.J. Gao, B.H. Ji, I.L. Jäger, E. Arzt, P. Fratzl, Materials become insensitive to flaws at nanoscale: Lessons from nature, Proc. Natl. Acad. Sci. U. S. A. 100 (10) (2003) 5597–5600.
[10] K.P. So, D. Chen, A. Kushima, M.D. Li, S.T. Kim, Y. Yang, Z.Q. Wang, J.G. Park, Y.H. Lee, R.I. Gonzalez, M. Kiwi, E.M. Bringa, L. Shao, J. Li, Dispersion of carbon nanotubes in aluminum improves radiation resistance, Nano Energy 22 (2016) 319–327.
[11] J.F. Ziegler, M.D. Ziegler, J.P. Biersack, Srim: The stopping and range of ions in matter (2010), Nucl. Instrum. Meth. Phys. Res. B 268 (11) (2010) 1818–1823. 19th International Conference on Ion Beam Analysis
[12] J. Winey, A. Kubota, Y. Gupta, A thermodynamic approach to determine accurate potentials for molecular dynamics simulations: thermoelastic response of aluminum, Model. Simul. Mater. Sci. Eng. 17 (5) (2009) 055004.
[13] D.W. Brenner, O.A. Shenderova, J.A. Harrison, S.J. Stuart, B. Ni, S.B. Sinnott, A second-generation reactive empirical bond order (rebo) potential energy expression for hydrocarbons, J. Phys. Condens. Matter 14 (4) (2002) 783.
[14] G.J. Martyna, M.L. Klein, M. Tuckerman, Nosé-Hoover chains: The canonical ensemble via continuous dynamics, J. Chem. Phys. 97 (4) (1992) 2635–2643, doi:10.1063/1.463940.
[15] M.M. Jin, P. Cao, M.P. Short, Thermodynamic mixing energy and heterogeneous diffusion uncover the mechanisms of radiation damage reduction in single-phase Ni-Fe alloys, Acta Mater. 147 (2018) 16–23.
[16] K. Nordlund, M. Ghaly, R.S. Averback, M. Caturla, T. Diaz de la Rubia, J. Tarus, Defect production in collision cascades in elemental semiconductors and FCC metals, Phys. Rev. B 57 (1998) 7556–7570, doi:10.1103/PhysRevB.57.7556.
[17] X.-M. Bai, A.F. Voter, R.G. Hoagland, M. Nastasi, B.P. Uberuaga, Efficient annealing of radiation damage near grain boundaries via interstitial emission, Science 327 (5973) (2010) 1631–1634, doi:10.1126/science.1183723.
[18] S. Nosé, A molecular dynamics method for simulations in the canonical ensemble, Molec. Phys. 52 (2) (1984) 255–268.
[19] W.G. Hoover, Canonical dynamics: Equilibrium phase-space distributions, Phys. Rev. A 31 (1985) 1695–1697, doi:10.1103/PhysRevA.31.1695.
[20] M. Norgett, M. Robinson, I. Torrens, A proposed method of calculating displacement dose rates, Nucl. Eng. Des. 33 (1) (1975) 50–54.
[21] C. Sun, D. Bufford, Y. Chen, M.A. Kirk, Y.Q. Wang, M. Li, H. Wang, S.A. Maloy, X. Zhang, In situ study of defect migration kinetics in nanoporous ag with enhanced radiation tolerance, Sci. Rep. 4 (2014) 3737.
[22] A. Vattré, T. Jourdan, H. Ding, M.-C. Marinica, M.J. Demkowicz, Non-random walk diffusion enhances the sink strength of semicoherent interfaces, Nature Commun. 7 (2016) 10424.
[23] M. Swenson, J. Wharry, The comparison of microstructure and nanocluster evolution in proton and neutron irradiated fe-9 % cr ods steel to 3 dpa at 500c, J. Nucl. Mater. 467 (2015) 97–112.
[24] E. Castillo, Extreme value theory in engineering, Elsevier, 2012.
[25] X. Yi, A. Sand, D. Mason, M. Kirk, S. Roberts, K. Nordlund, S. Dudarev, Direct observation of size scaling and elastic interaction between nano-scale defects in collision cascades, EPL (Europhysics Letters) 110 (3) (2015) 36001.
[26] J.D. Eshelby, The determination of the elastic field of an ellipsoidal inclusion, and related problems, Proc. Royal Soc. London A 241 (1226) (1957) 376–396, doi:10.1098/rspa.1957.0133.
[27] G.S. Was, Fundamentals of radiation materials science: metals and alloys, Springer, 2016.
[28] M. Jin, P. Cao, S. Yip, M.P. Short, Radiation damage reduction by grain-boundary biased defect migration in nanocrystalline Cu, Acta Mater. 155 (2018) 410–417.
[29] M. Jin, P. Cao, M.P. Short, Mechanisms of grain boundary migration and growth in nanocrystalline metals under irradiation, Scripta Mater. 163 (2019) 66–70.
[30] C.Y. Lu, L.L. Niu, N.J. Chen, K. Jin, T.N. Yang, P.Y. Xiu, Y.W. Zhang, F. Gao, H.B. Bei, S. Shi, M.-R. He, I.M. Robertson, W.J. Weber, L.M. Wang, Enhancing radiation tolerance by controlling defect mobility and migration pathways in multicomponent single-phase alloys, Nature Commun. 7 (2016) 13564.

Supplementary information

1. Synthesis methods of Al/CNTs composite

The uniform dispersion of carbon nanotubes (CNTs) into aluminum (Al) grains was achieved from the three main processes, (i) the CNT declustering, (ii) cold-welding and encapsulation, and (iii) interfacial bonding. As the high aspect ratio of CNTs typically entangles each other, forming clusters, we first introduce a declustering process using high-speed blades. The declustering process of CNTs on the surface of Al particles was performed by a high-speed blade blender (VM0104, Vita-Mix, USA) to unravel the tangled multiwalled carbon nanotubes (MWCNTs), (CM95, Hanwha Nanotech, Korea) for 20 min at max. 37,000 rpm. The SEM image of pristine CNT clusters and Al particles are shown inFig. S 1A and B respectively. The individual strand of CNTs with 5 wt% on the Al particle after declustering are shown in Fig. S 1C. The Al particles with declustered CNTs on the surfaces were cold-welded using a planetary ball miller (J.E. Powder, Korea) for 30 min at 250 rpm, as shown by the Al/CNT granule in Fig. S 1D (SEM of the surface of granule). The CNTs are completely encapsulated into Al particles. This ball mill process allows diluting the concentration of CNTs. The ball mill was completed in a glove box (M.O. Tech, Korea) under less than 1 ppm of oxygen and moisture to prevent oxidation. For the CNT volume calculation, a CNT density of 1.3 g/cm^3 was used. As a consequence of the cold-welding, CNTs are encapsulated in Al particles that were further consolidated under 40 MPa with spark plasma sintering (SPS, 50 t, 50 kW, Eltek, Korea) to form interfacial Al–C covalent bonds at 560 °C for 15 min (Fig. S 1E). The bulk Al/CNT composites were extruded to 8 mm in diameter with an extrusion ratio of 9:1 at 550 °C. The extruded samples were cold rolled to 2mm thickness at room temperature. The reduction ratio of each rolling pass was approximately 30%. We proceeded the annealing to release the residual stress for 24hrs at 400^{o}C under the ambient atmosphere.

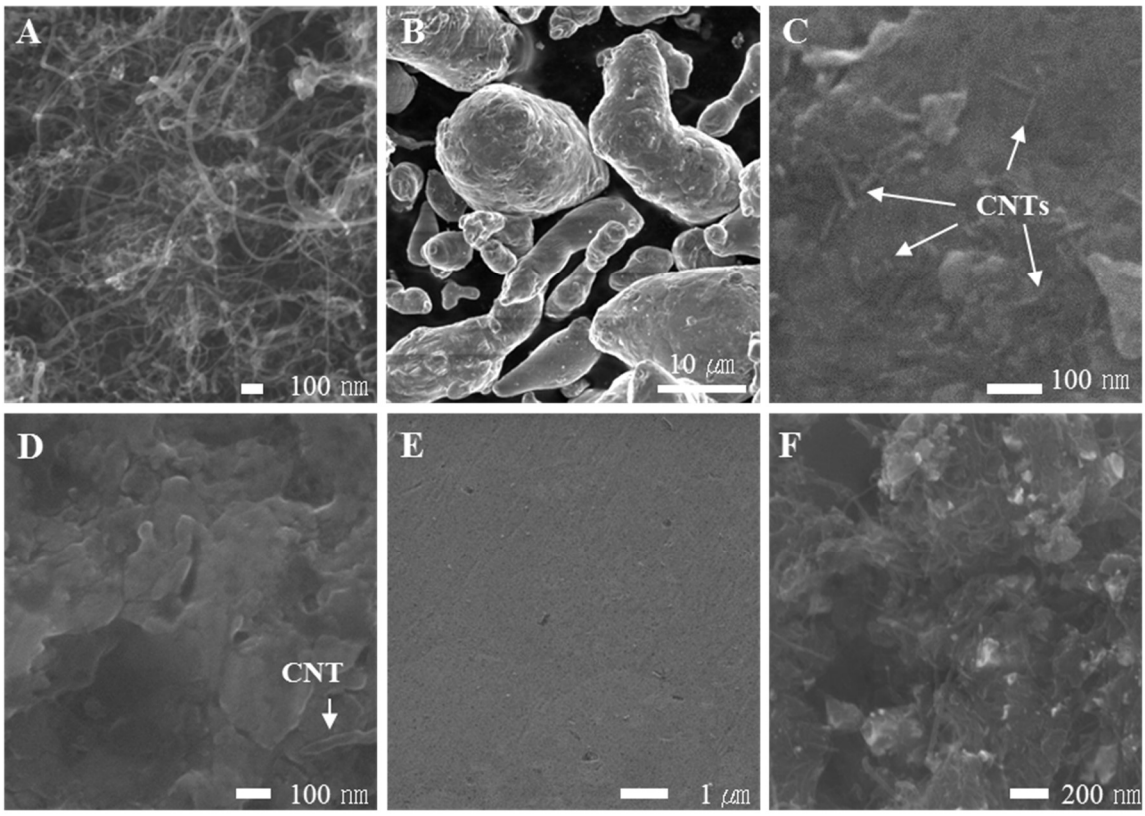

Fig. S 1 SEM images for each step. (A) Raw CNTs, (B) raw Al powder, (C) Al/CNT composite after 2 vol% CNT declustering process. Individual CNTs were visible on the surface of Al particles. (D) Master alloy after encapsulation of 0.4 vol% CNTs. (E) Al/CNT composite after SPS and extrusion, and (F) CNTs embedded inside Al, which appeared after acid etching. The diameter and length of MWCNTs were in the range of 10~30 nm and a few tens micrometers, respectively (A). The purchased gas-atomized aluminum powder was filtered by 200 meshes to have particle sizes less than 50 microns, as shown in (B). Individual CNTs were observed on the surface of Al particles after declustering process, as shown in (C). The declustered CNTs were embedded inside Al particles after an oxygen-free mechanical pulverization-assisted encapsulation process, as shown in (D). Al particles were fractured. The bare surface was exposed without oxidation during mechanical pulverization. The fractured Al particles were coalesced to each other during further pulverization process, forming CNT-embedded Al granules. The CNT morphology (1 μm length) was well maintained and detected after the final process, as shown (F).

SPS optimization

We optimized the sintering conditions to yield an Al+CNT composite with a density greater than 99% of the theoretical value by controlling the temperature and time, as shown in Fig. S 2A and B, respectively. To achieve a relative density of 99%, a sintering temperature of 560 ºC was used with a sintering time of 15 min at a pressure of 46 MPa. The increased relative density was easily obtained because CNTs were encapsulated inside the Al particles, i.e., no void volume was produced by CNT residence in the particle boundaries. Microstructural observations demonstrate

that the oxide layer on the Al granule surfaces was successfully disintegrated by the SPS process, forming discrete oxide nanoparticles, as shown in Fig. S 3A to C.[1]

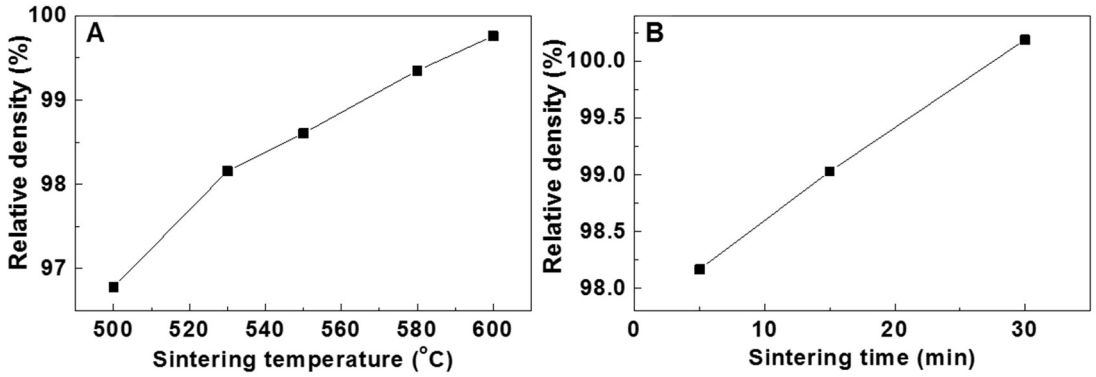

Fig. S 2 Sintering process-dependent relative density compared to that of the Al/CNT composite. (A) The sintering temperature- and (B) sintering time-dependent relative densities. The reference density was calculated by, $\rho_{\text{Ref.}} = \dfrac{\rho_{CNT}\rho_{Al}}{\rho_{CNT}m_{Al} + \rho_{Al}m_{CNT}}$ where ρ_{CNT}, ρ_{Al}, m_{CNT} and m_{Al} are CNT density, Al density, CNT weight fraction and Al weight fraction, respectively. A CNT density of 1.3 g/cm^3 was used. The relative density was obtained from experimental density divided by the reference density. The increased relative density to nearly to 100% was easily obtained because CNTs were encapsulated inside the Al particles, i.e., no dead volume was produced by CNT residence in the particle boundaries. To achieve high-density more than 99 % relative density, 580 ºC and 15 min of the sintering temperature and time were used.

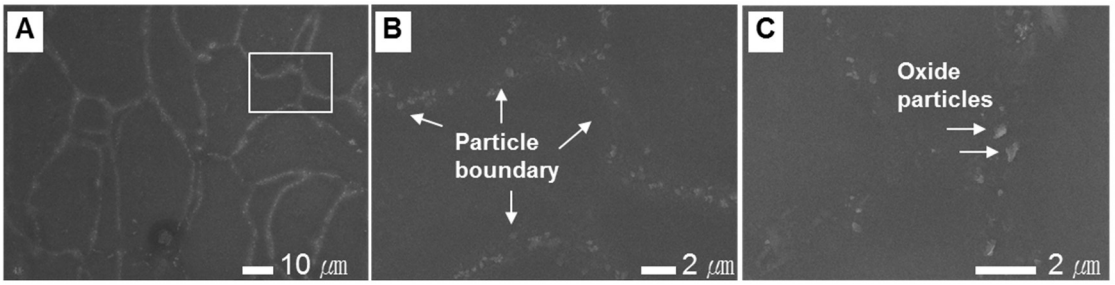

Fig. S 3 Microstructure observations after SPS at 580 ºC for 15 min with 2 vol% CNT. (A) A particle boundary trace indicated by white lines, (B) enlarged in (A), and (C) oxide nanoparticles. The oxide layer on the surface of Al granules was formed after encapsulation during sample transfer for SPS. Note that CNTs were already well dispersed inside Al granules. Microstructural observations demonstrate that the oxide layer on the encapsulated Al granule surfaces was successfully disintegrated by the SPS process, forming discrete oxide nanoparticles.

2. TEM sample preparation and observation

We have prepared samples for the transmission electron microscope (TEM) and intermittent voltage electron microscope (IVEM). Al samples with thickness ~100 nm were prepared using a focused ion beam (FIB) at MIT (Helios Nanolab 600 Dual Beam FIB Milling System) and at brook heaven national lab. The surface of the bulk samples deposited by platinum (Pt) to minimize the damage of the surface. The samples were shaped into a square block with 13 um of length, 5um of height, and 1um of thickness by Gallium (Ga+) ion beam. The square block was transferred to Cu TEM half grid and welded by Pt electron/ion beam deposition inside a scanning electron microscopy. We used an ion beam to thin the sample down to ~100nm of thickness. 30 keV of ion acceleration voltage was used at the initial thinning process and gradually reduce to 5 keV to minimize the damage of the samples. The thickness of the TEM lamella is 120 nm for pure Al and 70 nm for Al-CNT. To verify the location of CNT, we observe the samples in TEM (JEOL 2010F) with 200 keV acceleration voltage. Fig. S 4 A indicates the grain structure of the Al where the size of the grain is around 500nm~1um. The white circle indicates the location of the CNT. It shows the CNT is located inside the grain. The enlarged area of the white circle clearly shows the cylindrical cross-section of CNT and 3.3A of the intrinsic graphitic layers of the CNT, Fig. S 4C, indicating the damage is not significant during the synthesis process.

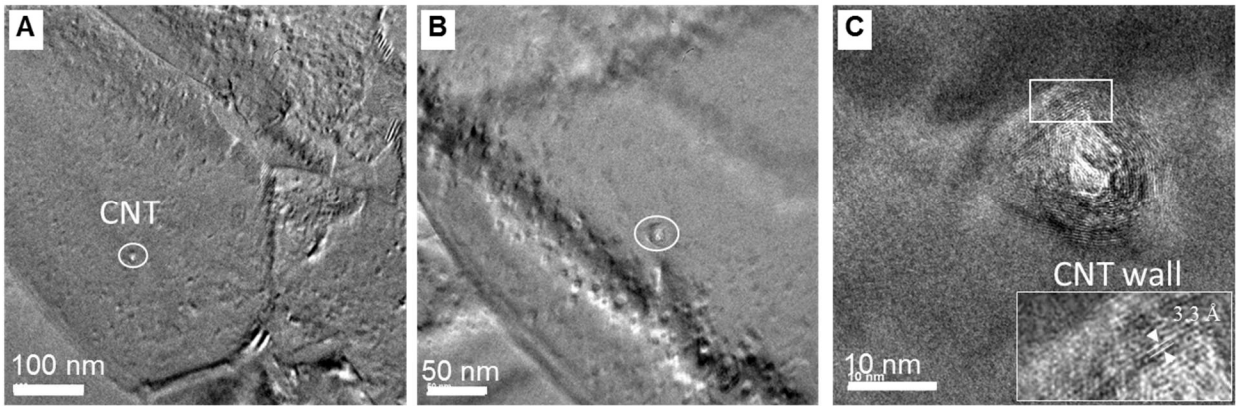

Fig. S 4 TEM image of the Al/CNT composite (A) grains of Al where the white circle indicate the location of CNT in grain, (B) enlarged area of white circle in (A), (C) structure of CNT, inset wall structure of the CNT, indicating 3.3 A of the graphitic interspacing layer.

SRIM calculation

The ion irradiation damage and depth profiles of Al foils were calculated by the software SRIM 2008[S1] using the "Kinchin-Pease quick calculation" mode and plotted in Fig. S **5**. Here, the displacement energy of Al was set 25 eV.[2] It can be seen that the damage profiles are non-uniform under ion irradiation, the damage by each sample is identified by the number of displacements per atom (DPA) at the damage zone inside samples.

The DPA was obtained by the following equation.

$$does\frac{ion}{cm^2}\times 1(\frac{1(number)}{10^{-8}(cm\cdot ion)})/\rho\left(\frac{g}{cm^3}\right)\cdot 6.02\times\frac{10^{23}}{mol}/(\text{atomic number}\left(\frac{\text{g}}{\text{mol}}\right))$$

Where the calculated 1 DPA in Al TEM lamella is the irradiation ion doses with $3.763\times10^{14}/cm^2$ at 100 keV and $6.02\times10^{14}/cm^2$ at 1 MeV.

A random C distribution was assumed for the SRIM estimation, but stopping by MWCNT is complex, and has been recently addressed.[3] Therefore, the geometrical factor of MWCNT has not been considered in this calculation.

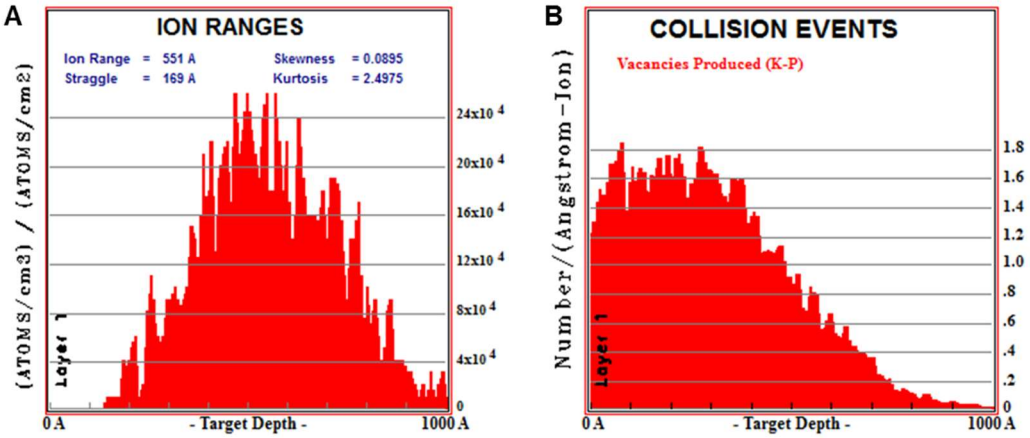

Fig. S 5. SRIM calculation of (A) ion ranges and (B) collision event under 100keV Kr^{++} ion into Al matrix

In-situ irradiation

The ion irradiations were performed in situ in a transmission electron microscope using the intermediate voltage electron microscopy (IVEM)-accelerator facility at Argonne National Laboratory where an ion accelerator is attached to a HITACHI H-9000 microscope. *In situ* Kr^{++} ion irradiation at 100 keV and 1 MeV was performed for pure Al and Al-CNT composites at room temperature. Kr^{++} ion irradiation was performed after a focused ion beam (FIB) extraction of TEM lamellae. The microscope was operated at 150 keV, and kept on during irradiation to record the microstructural evolution. The dose rate was $0.9\sim2.7 \times 10^{-3}$ DPA/s. A CCD camera was used to capture microstructural evolution during radiation at fifteen frames per second. The Stopping power and Range of Ions in Matter (SRIM)[6] simulation package was used to estimate the displacement damage profile and Kr^{++} ion distribution[7]. The detail irradiation condition is described in Table S1.

Table S1. Summary of Irradiation condition in pure Al and Al-CNT

Batch	Samples	Irradiation ion	Ion Acceleration	Electron voltage	Temperature	Dose rate
1	Pure Al	Kr++	1 MeV	150 KeV	RT	0.86×10^{-3} DPA/s
2	Al-1 wt% CNT	Kr++	100 keV	150 keV	RT	2.7×10^{-3} DPA/s
3	Al-1 wt% CNT	Kr++	1 MeV	150 keV	RT	1.6×10^{-3} DPA/s

3. Image process in IVEM

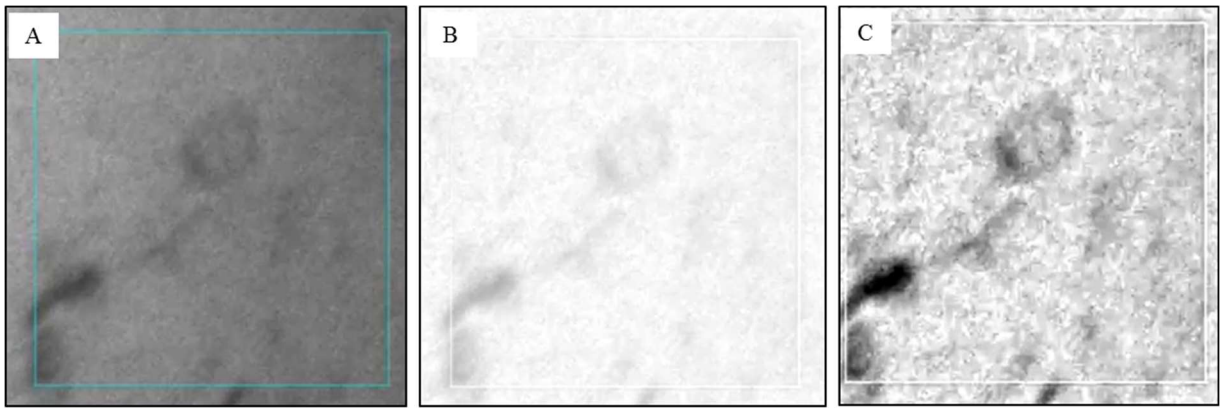

Fig. S 6 Image analysis procedure by using the program "image J." (A) Raw image from the IVEM, (B) background subtraction with 50 pixels of rolling ball radius, (C) the contrast was enhanced with the 0.3% saturated pixels.

TEM images were processed by several steps to clearly visualize the defect clusters by image J after irradiation. The background noise was subtracted at a rolling ball radius of 50 pixels (Fig. S 6B), and the contrast was enhanced at saturated pixels 0.3% (Fig. S 6C).

4. The volume fraction of the defects

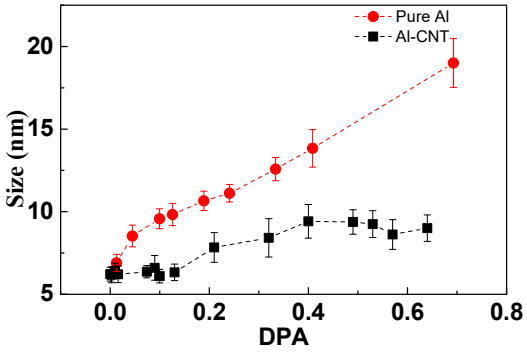

Fig. S 7 The average size of the defect.

The defects density were obtained from the IVEM video. The counted area in the TEM observation and TEM lamella thickness were used to convert the defect cluster density in volume. The original defect density of Al-CNT is higher than that of pure Al. However, the average size of defects in Al-CNT is smaller than that in pure Al as plotted in Fig. S 7

. The size difference is getting larger as DPA is higher at the pure Al. The defect density and the average defect size are used to convert the volume fraction of the defect in Fig. 2E.

The average defect sizes were converted into the average volume. All the detectable defects are approximated to be the sphere.

$$V_d = \frac{4}{3}\pi r^3$$

Where, V_d is the average volume of the defects, r is the average radius of the defects.

The volume fraction is extracted from the following.

$$V_f = \frac{V_d \times N}{At}$$

Where, V_f is the volume fraction of the defects, N is the number count of the defect from the IVEM, A is the area of the defects counting, and t is the thickness of the TEM lamella. The thickness of the TEM lamella is 120 nm for pure Al and 70 nm for Al-CNT. The volume percent of CNT in the detected area is about 0.4 vol% where the interface area of CNT is ~4400nm^2 and the surface area of the Al lamella is 2.07 × 10^5 nm^2. The surface area of Al lamella is ~50 times larger than the interface area between CNT and Al. Therefore, a strong driving force attracts the defect toward CNT.

5. Al3C4 transformation of CNT after irradiation

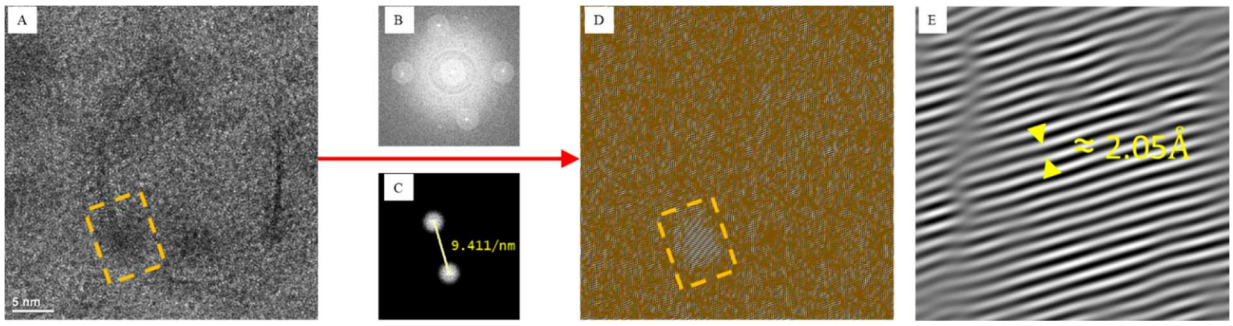

Fig. S 8 Microstructure of CNT after ~100 DPA irradiation. (A) TEM image at the CNT area. (B) FFT and (C) filtering of FFT, (D) recreation of filtered FFT, (E) inverse FFT from the orange square in A and D indicate Al_3C_4 lattice at the edge of CNT. This 2.05 Å value has considered the error of scale bar (≈ +4%)

The area where the irradiation occurs near the CNT was characterized through ex-situ TEM (Fig. S9). The circular shape was still observed after 100 DPA of Kr ion irradiation, suggesting the fossl of CNT. The Fast Fourier transformation (FFT) shows the location of Al_4C_3 at the edge of CNT in Fig. S 8 B~D. The inverse FFT image suggests that the lattice distance of 2.05 Å is the Al4C3 (0012).

6. Extreme value theory (EVT) analysis of defect size

From a fracture mechanics perspective, the large defects can be more damaging to mechanical properties than small ones and are crucial for radiation-induced material failure. Therefore, the tail behavior of defect size is of the central interest. The interesting question turns into how to use our sampled data on defect size to infer the tail features of underlying unknown defect distribution in Al and Al-CNT. The EVT, which is an analog of the central limit theorem, reveals that, if there are n independent random variables $X_1, X_2 \ldots, X_n$ from the same underlying distribution, the block

maximum $M_n = \max(X_1, X_2 \ldots, X_n)$ converges to Generalized extreme value (GEV) distributions when $n \to \infty$.

The GEV is a family of probability distributions by combing three distributions (Gumbel, Frechet and Weibull) into a single form. The probability density function for the GEV is

$$p(x|\xi, \mu, \sigma) = \frac{1}{\sigma}\exp\left(-\left(1+\xi\frac{x-\mu}{\sigma}\right)^{-\frac{1}{\xi}}\right)\left(1+\xi\frac{x-\mu}{\sigma}\right)^{-1-\frac{1}{\xi}}$$

with location parameter μ, scale parameter σ, and shape parameter $\xi \neq 0$. For the cases of $\xi = 0$, the density function becomes $p(x|\xi = 0, \mu, \sigma) = \frac{1}{\sigma}\exp\left(-\exp\left(-\frac{x-\mu}{\sigma}\right) - \frac{x-\mu}{\sigma}\right)$. Each type of distribution, determined by the sign of ξ, suggest different tail/extreme value behaviors of the underlying random variable.

We analyze the defect size distributions in Al and Al-CNT using EVT to deduce the extreme defect behaviors, and their radiation-resistance can be evaluated and compared. The defect size X_i in each TEM image is a random variable of interest, and all the detectable defects x larger than 3 nm are considered as block maximum for EV analysis. The probability distribution $p(x)$ is fitted to the GEV functions, aiming to deduce the tail behavior in Al and Al-CNT. To address the finite number of sampled data ($n \ll \infty$) and possible data correlation, we consider 95% confidence intervals for the GEV parameter estimates. The obtained results are shown in Fig. S9 with the following parameters

$$\xi = 0.06;\ \mu = 3.34; \sigma = 8.24; \quad \text{(Al)}$$
$$\xi = 0.01;\ \mu = 1.88; \sigma = 5.47; \quad \text{(Al-CNT)}.$$

The key value in GEV function is a shape parameter ξ, which decides the tail behavior – the tail type and its decay rate. If $k > 0$, the GEV is the Type II case (Frechet distribution), which has a heavy tail and decreases slowly such as a polynomial decay. If $k < 0$, it corresponds to Type III case (Weibull distribution) whose tail are finite. For $k = 0$, it is Type I (Gumbel distribution) whose tail decreases exponentially – a light tail with fast decay. Both ξ values in Al and Al-CNT are positive, implying that the underlying defect distributions have a heavy tail, such as polynomial decay which is consistent with previous experimental results on radiation-induced defects size distribution. Al-CNT with smaller ξ suggests fast tail decay, implying better radiation-resistance

to defect size growth. The larger location and scale parameters in Al indicate the large defects are more frequent than that in Al-CNT.

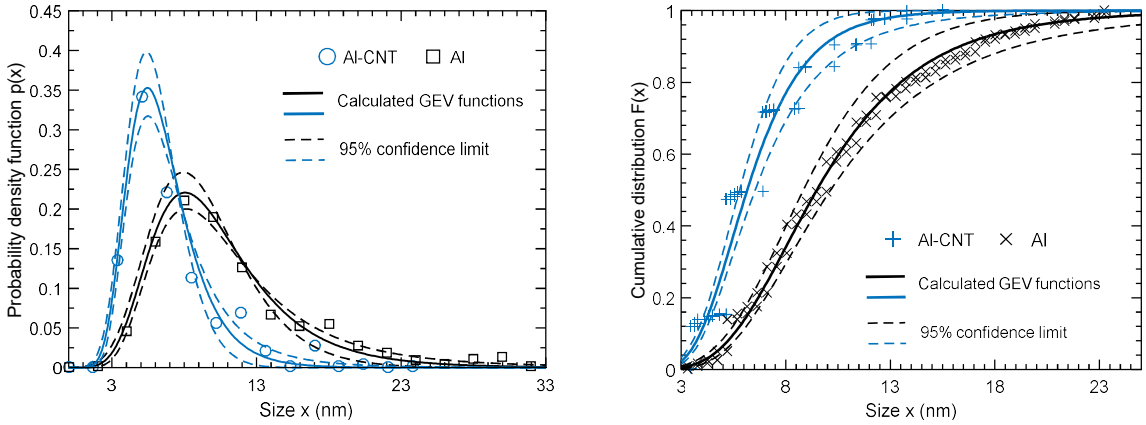

Fig. S9 (left) Probability density distributions and (right) the corresponding cumulative density distributions. The solid lines are calculated GEV functions with 95% confidence intervals indicated by dashed lines.

7. Tensile stress filed induced by aluminum carbide inclusion

To solve the stress and strain field in the Al matrix, we assume the CNT undergoes a uniform deformation due to a chemical reaction between C and Al as illustrated in Fig. S 10. If there is no confinement of Al matrix, the aluminum carbide C-Al have a uniform eigenstrain ε_r^* and experience zero external stress. In reality, both the C-Al and Al matrix will deform and experience tensile stress. Let's define constrain strain ε_r^c on the interface after relaxation, which can be estimated by Eshelby inclusion. For simplicity, we will compute the general trend of strain field in the matrix as a function of distance from C-Al with any given ε_r^c.

Assume the matrix is isotropic medium, undergoing linear elastic deformation. The length of CNT is long, much larger than its diameter, then it becomes a 2D plane strain problem. We first find the displacement field in the matrix and obtain the explicit solution for the strain and stress. Using polar coordinates, the displacement field be expressed as $\boldsymbol{u}(r,\varphi) = u_r\,\boldsymbol{e}_r + u_\varphi\,\boldsymbol{e}_\varphi$. As the displacement field does not depend on φ, so that it can be written as

$$\boldsymbol{u} = u_r\,\boldsymbol{e}_r \quad (1)$$

Staring from the electrostatic equation,

$$(\lambda + \mu)\nabla\nabla\bullet\mathbf{u} + \mu\nabla^2\boldsymbol{u} = -\mathrm{f}$$

where λ and μ are Lamé parameters. Given the identity $\nabla(\nabla\bullet\mathbf{U}) - \nabla \times (\nabla \times \mathbf{u}) = \nabla^2\boldsymbol{u}$, the electrostatic equation becomes

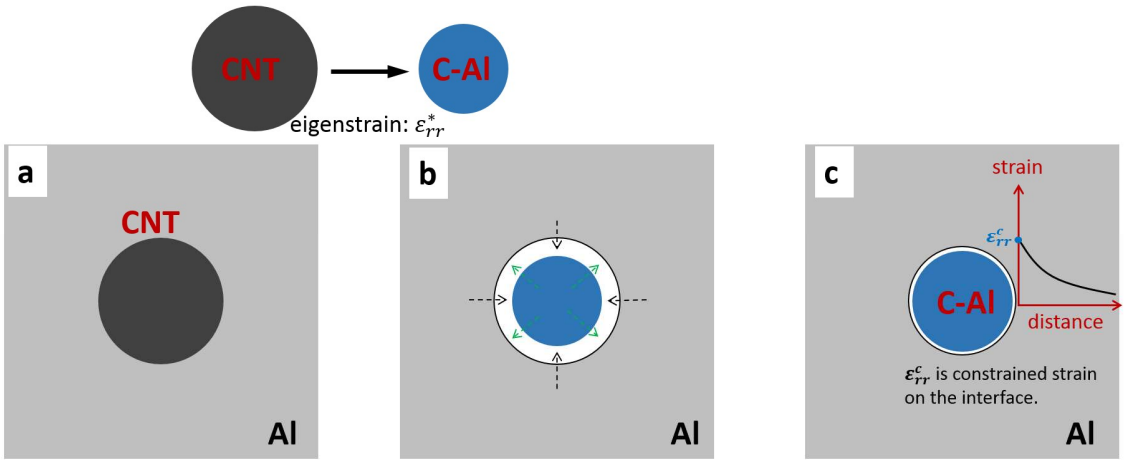

Fig. S 10 schematic carton view of C-Al reaction induced stress filed in Al matrix. (a) Initial Al-CNT configuration. (b) C and Al have chemical reactions forming aluminum carbide. The eigenstrain $\boldsymbol{\varepsilon^*_{rr}}$ represents the volume shrinkage due to the formation of aluminum carbide. (c) The relaxed system with stress/strain filed generated by $\boldsymbol{\varepsilon^*_{rr}}$, where $\boldsymbol{\varepsilon^c_{rr}}$ is the constrained strain on the interface.

$$(\lambda + 2\mu)\nabla\nabla\bullet\mathbf{u} - \nabla \times (\nabla \times \mathbf{u}) = -\mathrm{f}$$

It can be derived that $\nabla \times (\nabla \times \mathbf{u}) = \mathbf{0}$, and here we ignore the body force f, the above equation can be written as

$$\nabla\nabla\bullet\mathrm{u} = 0, \quad \text{i.e.} \quad \frac{\partial}{\partial r}\left(\frac{1}{r}\frac{\partial(ru_r)}{\partial r}\right) = 0$$

Solving the above equation obtains $u_r = \frac{A}{r} + Br$. We then apply two boundary conditions:

1. When $r \to \infty$, the displacement $u_r \to 0$.

$\Longrightarrow \quad B = 0.$

2. At interface r = a (where a is radius of include), $\varepsilon_{rr} = \varepsilon^c_{rr}$

$$\varepsilon_{rr}|_{r=a} = -\frac{A}{a^2} = \varepsilon^c_{rr} \ (\text{with } \varepsilon_{rr} = \frac{\partial u_r}{\partial r} = -\frac{A}{r^2})$$

$\Longrightarrow A = -a^2\varepsilon^c_{rr}.$

Finally, we obtain the stress and strain relationship, and the corresponding stress file in Fig. S 11:

$$\boldsymbol{\varepsilon_{rr} = a^2 \varepsilon_{rr}^c / r^2;}$$

$$\boldsymbol{\sigma_{rr} = 2\mu \frac{a^2 \varepsilon_{rr}^c}{r^2} = \frac{E}{1+v} * \frac{a^2 \varepsilon_{rr}^c}{r^2}.}$$

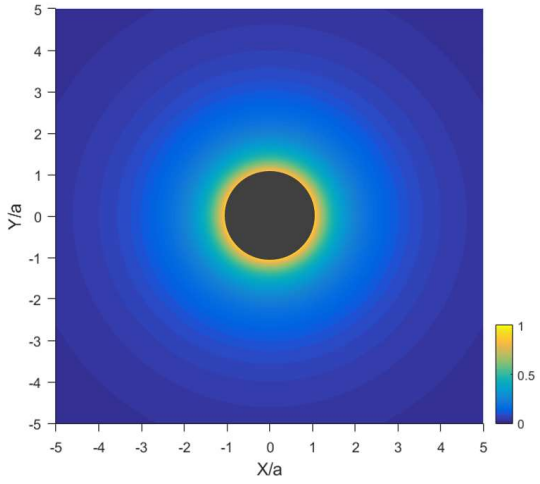

Fig. S 11 Stress field in Al matrix. The parameter represents the aluminum carbide radius. The magnitude of tensile stress is normalized by $\boldsymbol{2\mu\varepsilon_{rr}^c}$.

Movies

Movie 1. The initial moment of Kr^{++} ion 100 keV irradiation near the CNT. When Kr ion starts to irradiate on the TEM lamella, the original visible defects are disappeared to 0.01 DPA. As Kr ion further irradiate, new defects start generated. At the higher than 0.09 DPA, defects and loops start to move as stress build-up due to the accumulation of defects.
http://li.mit.edu/S/KangPyoSo/Upload/initialAl-CNT.avi

Movie 2. Biased defect loop migration toward CNT at 1.56DPA under 100 keV Kr ion irradiation.
http://li.mit.edu/S/KangPyoSo/Upload/LinedefectAl-CNT.avi

Movie 3. Molecular dynamic simulation of the biased the defect migration
http://li.mit.edu/S/KangPyoSo/Upload/MDAl-CNT-defects.avi

Movie 4. Defects generation and stress build-up at the CNT and GB under the 1MeV Kr ion irradiation. The area near CNT has less accumulation of defects are the biased preferential defect draft occurs which

limits the total density of defects as shown in Fig. 4A. However, the area near GB shows dynamic defects evolution and migration, indicating more defect accumulation that area near CNT.

http://li.mit.edu/S/KangPyoSo/Upload/CNT-GB.avi

Movie 5. 70 KeV Kr^{++} ion irradiation. The ion dose is $383 \times 10^{14}/cm^2$ which is about ~100DPA. The video indicates the Kr gas accumulation near CNT and diffuse to CNT internal and eventually disappeared.

http://li.mit.edu/S/KangPyoSo/Upload/KrimplementationCNT.avi

Reference

1. G. Q. Xie, O. Ohashi, T. Yoshioka, M. H. Song, K. Mitsuishi, H. Yasuda, K. Furuya & T. Noda. Effect of interface behavior between particles on properties of pure al powder compacts by spark plasma sintering. *Mater Trans* **42**, 1846-1849, (2001).
2. Z. A. Munir, U. Anselmi-Tamburini & M. Ohyanagi. The effect of electric field and pressure on the synthesis and consolidation of materials: A review of the spark plasma sintering method. *J Mater Sci* **41**, 763-777, (2006).
3. J. E. Valdés, C. Celedon, R. Segura, I. Abril, R. Garcia-Molina, C. D. Denton, N. R. Arista & P. Vargas. Energy loss distribution of proton beams at normal incidence on multi-walled carbon nanotubes. *Carbon* **52**, 137-144, (2013).
4. N. ASTM. E521 (1996) standard practice for neutron radiation damage simulation by charged-particle irradiation. *Annual Book of ASTM Standards* **12**.
5. R. E. Stoller, M. B. Toloczko, G. S. Was, A. G. Certain, S. Dwaraknath & F. A. Garner. On the use of srim for computing radiation damage exposure. *Nuclear instruments and methods in physics research section B: beam interactions with materials and atoms* **310**, 75-80, (2013).
6. Y. Wang, Z. Pan, Y. Ho, Y. Xu & A. Du. Nuclear instruments and methods in physics research section b: Beam interactions with materials and atoms. *Nuclear Instruments and Methods in Physics Research B* **180**, 251-256, (2001).
7. J. F. Ziegler & J. P. Biersack. Srim-2008, stopping power and range of ions in matter. (2008).